High Temperature Corrosion of Materials (2026) 103:79
https://doi.org/10.1007/s11085-026-10440-z

RESEARCH

High temperature oxidation behaviour of compositionally complex Ta–Mo–Cr–Ti–Al alloy in steam atmosphere

Björn Schäfer[1] · Michael Dürrschnabel[1] · Carsten Schroer[1] · Chongchong Tang[1] · Fabian Lanoy[2] · Emma White[2] · Mathias Galetz[2] · Bronislava Gorr[1]

Received: 19 May 2026 / Revised: 9 July 2026 / Accepted: 13 July 2026

Abstract

The oxidation behaviour of TaMoCrTiAl in steam at 900–1100 °C has been investigated by thermogravimetric analysis of oxidation kinetics and detailed cross-sectional SEM and TEM characterization of the multilayered oxide scales formed during exposure. Experiments point to the significance of both outward diffusion of metal cations and inward transport of oxidizing species, whereas the latter becomes increasingly dominant with increasing exposure times. Based on these findings, a mechanistic oxidation model for TaMoCrTiAl in steam is proposed and compared with the oxidation behaviour in air. In contrast to oxidation in synthetic air, the (Cr, Ta, Ti)O_2 layer typical for TaMoCrTiAl is absent, but formation of (Ti, Ta)O_2 observed, with impact on both formation of external oxide and internal corrosion.

Keywords Refractory high entropy alloy · Rutile-type complex oxide · High temperature steam oxidation · Thermogravimetry

Introduction

Refractory high-entropy alloys (RHEAs) have received attention as a next-generation of structural materials for applications at 1000 °C and clearly higher, because of their superior high-temperature strength and, as frequently reported, sluggish diffusion [1, 2, 3]. Especially in the Ta–Mo–Cr–Ti–Al system, a reasonably high melting point and, therefore, conservation of strength, may be combined with excellent oxidation resistance [4, 5], which is important for applications such as in the classic gas turbines found in aviation or power generation, as well as in emerging hydrogen-based energy systems, such as hydrogen combustion engines and fuel cells, where materials are exposed to high-temperature, steam-rich environments. As for the equimolar variant TaMoCrTiAl the key feature in oxide scales formed in air is a complex rutile-type

Extended author information available on the last page of the article

Published online: 25 July 2026

(Cr, Ta, Ti)O_2, which has been identified the major contributor to oxidation resistance [4, 5]. However, for practical applications, further reactive species, notably sulphur or carbon-containing ones, also may have to be considered. In connection with the proposed transition to a hydrogen economy, it is the high content of water vapour in hydrogen-combustion atmospheres that may possibly interfere with the formation of a protective oxide scale.

The influence of water vapour, or steam, on the oxidation behaviour of TaMoCrTiAl and related alloys is largely unexplored. In particular, the response of (Cr, Ta, Ti)O_2 has not yet been addressed in detail, though it could be argued that this response will show similarity to the behaviour of rutile-type TiO_2 in steam environments. The prominent changes observed in humid in comparison to dry atmosphere are [6–12]: (i) enhanced outward diffusion of cations through a rutile TiO_2 scale; and (ii) accelerated inward transport of oxygen via hydroxyl (OH^-) ions, which exhibit higher mobility compared to oxygen anions.

In the present study, oxidation of equimolar TaMoCrTiAl in steam is investigated by means of thermogravimetric and subsequent surface and cross-sectional analysis. Testing in steam is performed at 900–1100 °C, for durations between 2 and 100 h. The comparison with complementary experiments in air at 1000 °C is intended to support addressing the following questions:

(1) How does steam affect the phase constitution, structure and growth kinetics of the formed oxide scale?
(2) What are the dominant mass-transport phenomena and how does their relative contribution evolve with time?
(3) How does steam particularly influence the formation of (Cr, Ta, Ti)O_2, the oxide determining the excellent oxidation resistance of TaMoCrTiAl in air?

Experimental Procedures

The equimolar alloy TaMoCrTiAl was melted from granules of the respective elements (Ta, 99.9%; Ti, 99.7%; Mo, 99.97%; Cr, 99.94%; Al, 99.9%) with mass ratio that corresponds to the intended composition, i.e. each 20 at%. Arc melting was performed under Ar cover gas (around 0.6 atm) in an arc melter (model AM/0,5 Arc melting furnace by Edmund Bühler GmbH) with a water-cooled copper mould. The produced alloy button was flipped and remelted six times to ensure a homogenous composition. The dendritic microstructure formed during solidification after the arc melting was destroyed by a homogenization heat treatment (20 h at 1500 °C, 100 K/h heating and cooling rate) in a tube furnace (RHTC, Nabertherm GmbH) under flowing Ar. Spongy titanium was used as a getter to reduce oxygen and nitrogen partial pressure during the heat treatment.

The characterisation of the finished alloy has already been described in detail in a previous publication [13]. The chemical composition of the alloy measured both by inductively coupled plasma optical emission spectroscopy (ICP-OES) and standardless energy dispersive X-ray spectroscopy (EDX) is listed in Table 1. Expected uncer-

Table 1 Chemical composition in at% of the alloy TaMoCrTiAl: Results from ICP-OES and standard-less EDX analysis

Method	Ta	Mo	Cr	Ti	Al	O	*N*
ICP-OES	20.3	20.3	19.7	20.4	19.2	<0.1	<0.1
EDX	17.9	16.6	22.0	21.0	22.6		

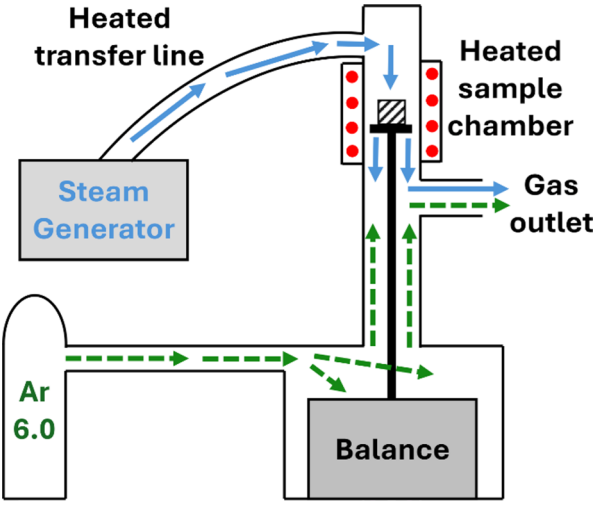

Fig. 1 Schematic illustration of the oxidation experiment setup. Blue arrows: steam flow, Green arrows: protective Ar flow

tainties are <0.1 at% (ICP-OES) and <3 at% (standardless EDX; with the exception of Mo, where it is <5 at%).

To determine the oxidation behaviour of TaMoCrTiAl, samples of the alloy with approximate dimension 5 × 5 × 2 mm, surface ground to #1200 and cleaned with ethanol in an ultrasonic bath were prepared. The thermogravimetric setup for the oxidation experiments is shown schematically in Fig. 1. The samples were exposed to flowing steam (2 g h^{-1} ≙ 41.5 ml min^{-1}) without carrier gas in a thermogravimetric system (STA 449 F3 Jupiter, Netzsch-Gerätebau GmbH). The steam atmosphere is provided by a direct steam evaporator (ASTEAM DV2, ADROP Feuchtemeßtechnik GmbH) from deionized, deaerated laboratory water. Under thermodynamic equilibrium, the oxygen partial pressure in steam resulting from water dissociation at 1000 °C and a total pressure of 1 bar is in the order of 10^{-4} mbar [14], which is high enough to form all oxides relevant to TaMoCrTiAl such as Cr_2O_3, TiO_2, Ta_2O_5, MoO_3, Al_2O_3 and (Cr, Ta, Ti)O_2 [5, 14]. The impurity level of oxygen in Ar gas used to protect the balance of the thermogravimetric setup is $5 \cdot 10^{-3}$ mbar. The argon gas is not directed past the sample; however, a slight leakage flow of oxygen from the argon gas to the sample cannot be ruled out. Therefore, the actual oxygen partial pressure might have been slightly higher than 10^{-4} mbar, which, however, does not compromise the statement as to oxide stability. During oxidation experiments, mass change was recorded as a function of time. Exposure times are 2, 48, 72 and 100 h for 1000 °C, and 72 h for 900 and 1100 °C. For comparison an additional oxidation experiment was performed in synthetic air (20.5 vol.-% O_2, 79.5 vol.-% N_2, 100 ml/min) at 1000 °C for 72 h. For each combination of atmosphere, temperature and time, one sample is tested.

To gain insights into the transport processes and growth directions of the respective layers of the external scale with respect to the initial sample surface, three Pt markers were applied to the surface of an TaMoCrTiAl sample which was subsequently exposed to steam at 1000 °C for 48 h. To investigate the protective properties of the inner sublayers of the external oxide scale, a discontinuous oxidation experiment as schematically shown in Fig. 2 was conducted. After 72 h exposure to steam at 1000 °C the outer layers of the external oxide scale (TiO_2, $(Al, Cr)_2O_3$, Al_2O_3) were removed mechanically by grinding and the sample subsequently exposed to steam for additional 24 h at 1000 °C.

For cross-section analysis, oxidized samples were wrapped in Cu and Al foil before embedding in conductive resin and grinding to #4000, followed by 1 µm polish. The cross-sections of the oxide scales were analysed via back-scatter electron (BSE) images, supplemented by EDX element mapping and line measurements in a Zeiss MERLIN scanning electron microscope (SEM). The SEM is operated with an acceleration voltage of 10 keV and beam current between 1 nA and 5 nA. The thickness of distinguishable layers in the oxide scales was assessed using ImageJ, by at least 30 measurements in BSE images taken from different locations on the sample.

For the oxide scales formed on TaMoCrTiAl during 72 h exposure to steam, a lamella for investigation in the transmission electron microscope (TEM) is prepared by milling with Ga^+ ions in a dual-beam focused ion beam - scanning electron microscope (FiB-SEM, Zeiss Auriga). The TEM and scanning TEM (STEM) investigations are conducted in a FEI Talos F200X operated with 200 kV acceleration voltage. The instrument is equipped with an X-FEG high-brightness electron gun as well as several detectors for STEM imaging: a Thermofisher Ceta 16 M CCD camera, a Super-X EDX detector, and a Gatan Enfinium SE spectrometer. Conventional TEM images and diffraction patterns are acquired using the Ceta camera. The orientation of the diffraction pattern is determined using the software SingleCrystal. Electron energy loss spectroscopy (EELS) is employed to track the oxidation states of the cations in the oxides. The Ti-$L_{2,3}$, O-K, and Cr-$L_{2,3}$ ionisation edges are captured in a single spectrum with the core-loss region set between 400 and 600 eV at 0.1 eV/channel. For the Ta-$M_{4,5}$ edge, the energy-loss range is set between 1650 and 2300 eV, with a dispersion of 0.25 eV/channel. Low-loss EELS spectra, recorded simultaneously with core-loss data in DualEELS mode, are used for energy-loss calibration and to determine the relative sample thickness t/λ, ensuring that $t/\lambda < 1$ for all analysed spectra. Quantification of the EELS spectra is performed using the built-in cross sections provided by the software Digital Micrograph.

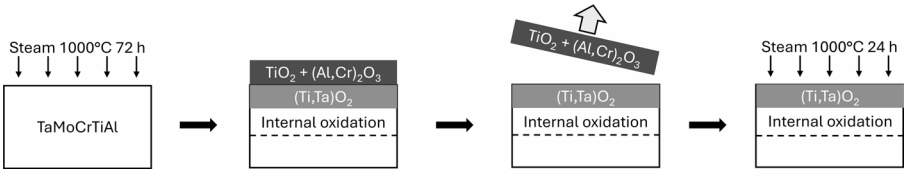

Fig. 2 Schematic illustration of the discontinuous oxidation experiment. (A more detailed description of the general structure of the oxide scale is presented in the results section.)

Results

Structure of oxide scales

The exposure of TaMoCrTiAl to steam at 900–1100 °C generally leads to the formation of an external oxide scale with layered structure and a pronounced internal oxidation zone (IOZ), as exemplified in Figs. 3 and 4 (1000 °C, 72 h in both cases). Exposure temperature primarily affects the thickness rather than the presence or structure of the individual layers. The outermost is rutile TiO_2 (marked as Nr. 1 in Fig. 4) followed by (Al, Cr)$_2O_3$ solid solution (Nr. 2 in Fig. 4), with both layers showing some porosity. The ratio between Al and Cr varies for individual (Al, Cr)$_2O_3$ grains but the Al content is usually higher. Below the (Al, Cr)$_2O_3$, a layer of Al_2O_3 is often observed (Nr. 3 in Fig. 4). However, this layer is very thin and discontinuous. These three layers (TiO_2, (Al, Cr)$_2O_3$ and Al_2O_3) are collectively referred to as outer oxide layer in the following. Beneath the outer oxide layer, a continuous layer of the rutile-type complex oxide (Ti, Ta)O_2 is observed, which can be divided into two sublayers: an outer sublayer, adjacent to the Al_2O_3 (or (Al, Cr)$_2O_3$), without any visible inclusions or pores (Nr. 4 in Fig. 4) and an inner sublayer with a few tens of nm sized Mo-rich metallic Mo inclusions and some tiny Al_2O_3 oxide inclusions (Nr. 5 in Fig. 4) close to the interface of external scale/IOZ. The latter is referred to as (Ti, Ta)O_2 + Mo in the following. The interface between the two sublayers of the (Ti,

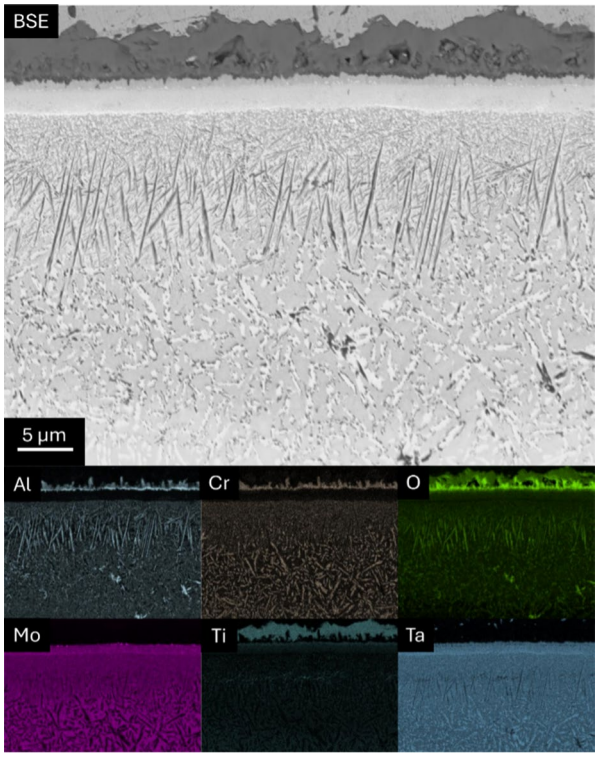

Fig. 3 BSE cross-section image of the oxide scale formed on TaMoCrTiAl after exposure to steam at 1000 °C for 72 h and corresponding EDX elemental maps

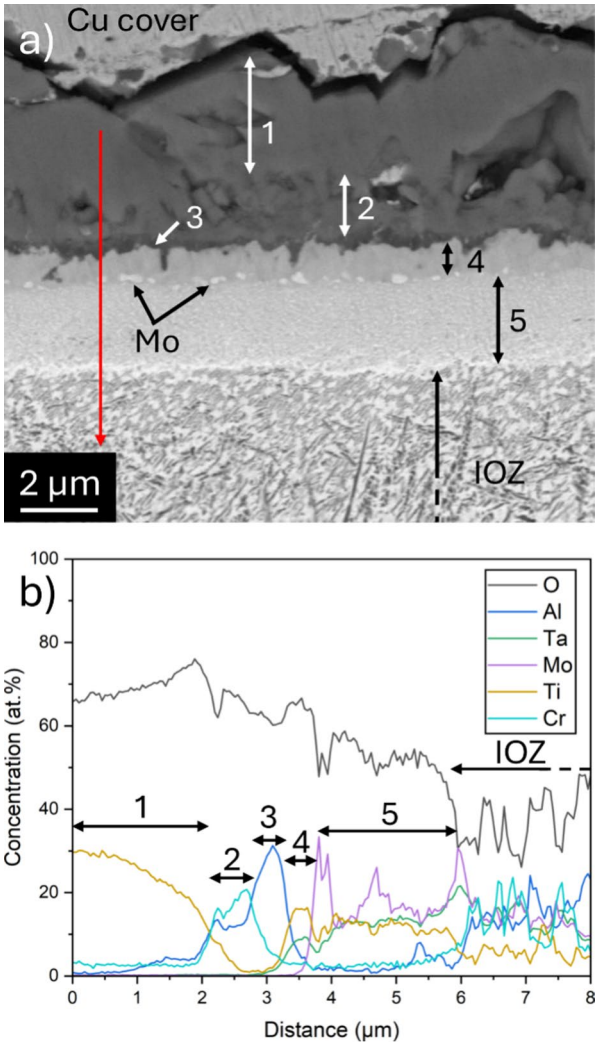

Fig. 4 **a** Detail BSE cross-section image of the external oxide scale formed on TaMoCrTiAl after exposure to steam at 1000 °C for 72 h. Identified layers are rutile TiO_2 (1), $(Al, Cr)_2O_3$ (2), Al_2O_3 (3), (Ti, Ta)O_2 (4), (Ti, Ta)O_2+Mo (5) and internal oxidation zone (IOZ). **b** EDX-line scan across the external oxide scale at position marked by red line in (**a**)

Ta)O_2 is usually marked by a series of bigger Mo inclusions, whereas the interface of (Ti, Ta)O_2 and IOZ features a Mo enrichment in many areas, visible as bright line in the BSE-images (Fig. 3). The Ti to Ta ratio is not constant throughout the (Ti, Ta)O_2 layer. In general, the Ta content increases toward the internal oxidation zone (Fig. 4b).

The oxide precipitates in the internal oxidation zone are predominantly Al_2O_3 and additionally some TiO_2 in case of longer exposure times (t>48 h at 1000 °C), as qualitatively identified by EDX (Fig. 4). Like the external scale, the IOZ can be divided into three sublayers, however with less defined interfaces and more gradual transitions between the individual sublayers. The precipitates within the outer sublayer beneath the (Ti, Ta)O_2 are on average rather small, compact in shape and mostly Al_2O_3. Ti is depleted in this layer (Fig. 5). The central sublayer additionally exhibits bigger, elongated Al_2O_3 precipitates, with the long axis approximately perpendicular

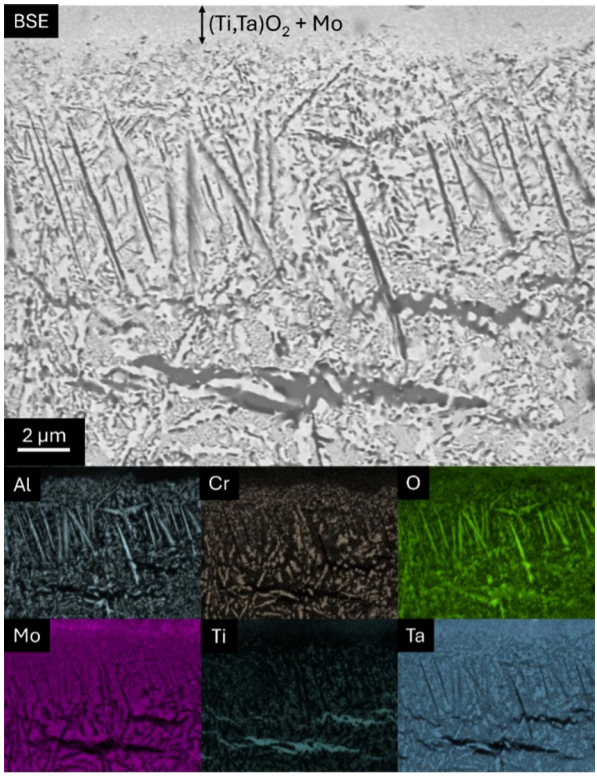

Fig. 5 Detail BSE cross-section image and corresponding EDX elemental mapping of the IOZ formed on TaMoCrTiAl after exposure to steam at 1000 °C for 100 h

to the alloy surface, and for longer exposure times also TiO_2 with long axis parallel to the latter (Fig. 5). In the innermost sublayer solely Al_2O_3 is present as precipitate, again with rather small average size and compact shape (Fig. 5). All oxide precipitates preferentially form at the grain boundaries of the Laves phase that additionally forms during the exposure, featuring higher density and bigger size of oxide precipitates at these interfaces compared to within the matrix.

As observed previously during oxidation in air at 1000 °C [4, 5, 13, 15, 16], the microstructure of the alloy changes due to the formation of additional Cr_2Ta Laves-phase precipitates within the matrix grains.

TEM analysis of (Ti, Ta)O_2 layer

Based on the results obtained for exposure to air [4, 5, 13, 15, 16], the layer of complex rutile oxides is supposed to be the main contributor to the oxidation resistance and therefore subject to a more detailed examination using TEM. Figure 7b shows a more detailed EDX mapping of the external oxide scale with the (Ta, Ti)O_2 layer located in the centre of the mapping. Selected area electron diffraction (SAED) pattern, obtained for both sublayers of this complex oxide and the Mo-rich inclusions contained therein are shown in Fig. 7c, overlain with corresponding SAED pattern of $TiTaO_2$ (with fixed 1:1 Ti/Ta ratio) and metallic Mo, calculated from literature data provided by the SingleCrystal software. Both analyses confirm the presence of

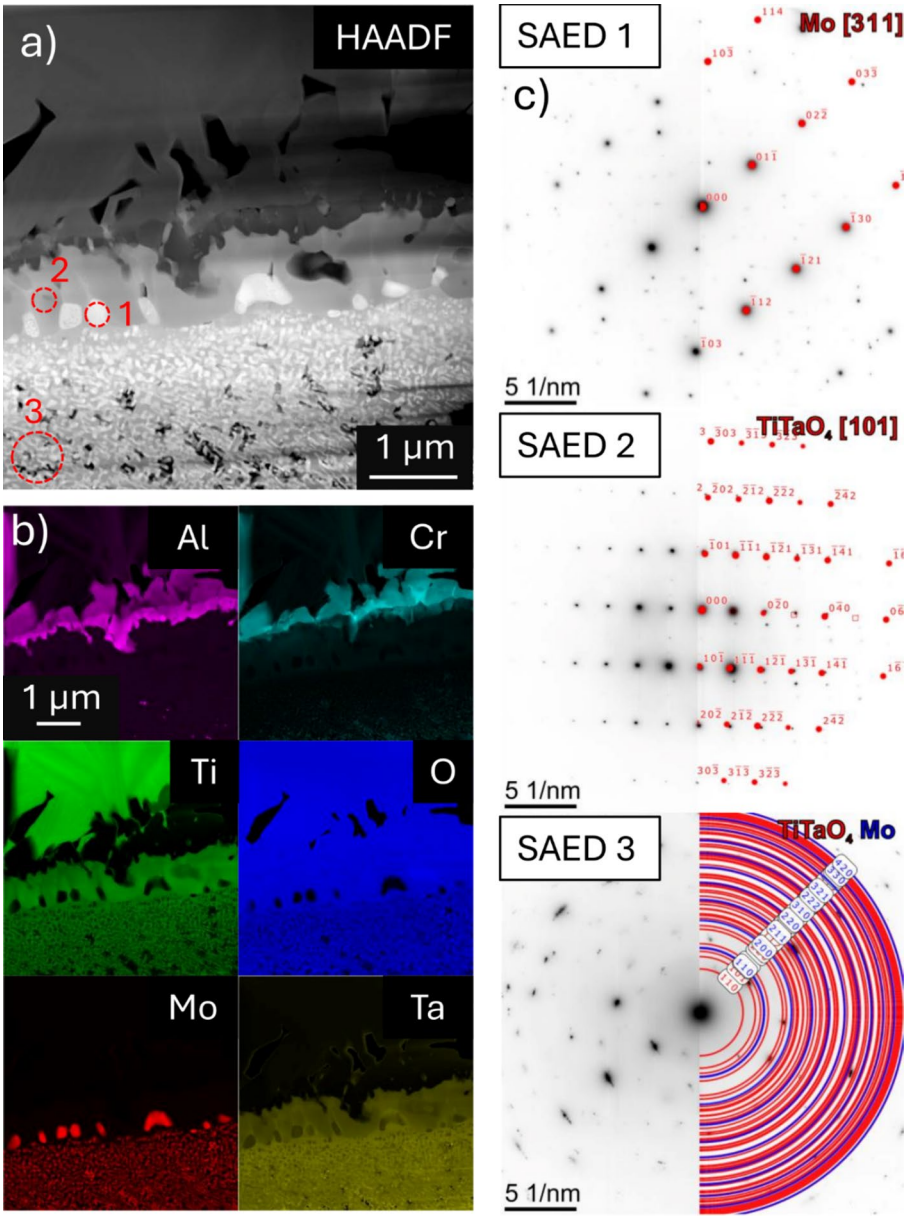

Fig. 6 TEM analysis of (Ti, Ta)O2 layer formed on TaMoCrTiAl during 72 h exposure to steam: a HAADF-STEM micrograph and b corresponding EDX elemental mapping, c) SAED pattern obtained from positions marked by red circles in a), overlain with patterns of TiTaO4 and Mo calculated from literature data

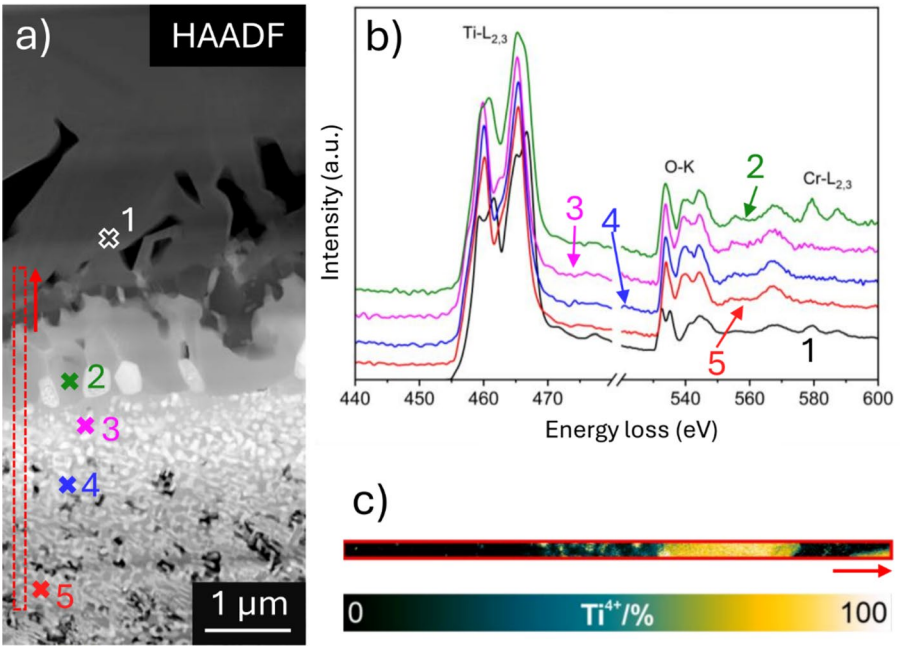

Fig. 7 Results from TEM investigation of complex oxide layers formed on TaMoCrTiAl after 72 h at 1000 °C in steam: a STEM-HAADF image with spots of EELS measurements, b EELS spectra in the range 400 to 600 eV showing Ti-L2,3, O-K and Cr-L2,3 peaks, c distribution of Ti valence within the (Ti, Ta)O2 layer.

rutile-type (Ti, Ta)O_2 and the metallic nature of the Mo-rich inclusions. Unlike to oxidation in air, no (Cr, Ta, Ti)O_2 layer is observed. Figure 7 shows the results of the EELS measurements for the energy-loss range from 450 to 600 eV where the Ti-$L_{2,3}$, O-K and Cr-$L_{2,3}$ edges are located. The energy loss near-edge structure (ELNES) of the Ti-$L_{2,3}$ and O-K edge differ for (Ti, Ta)O_2, most notably for the Ti-$L_{2,3}$ edge. The shape of the Ti-$L_{2,3}$ peak in curves corresponding to upper parts of the scale (curves 1 and 2 in Fig. 7b) corresponds mostly to those of Ti with formal + 4 valence, while the shape of the peaks in the curves corresponding to lower parts of the (Ti, Ta)O_2 layer (curves 3, 4 and 5) indicate + 3 valence [17, 18].

The $Ti^{4+}/\Sigma Ti$ ratio was determined using the single-window edge-onset method of Zanetta et al. [19]. After background subtraction, plural scattering removal, and continuum subtraction, each spectrum was normalized to its individual maximum intensity, which corresponds to the d peak of the Ti-$L_{2,3}$ edge. The integrated intensity within a 2 eV-wide window positioned from 455 to 457 eV at the onset of the Ti-L_3 edge was then measured. This onset intensity decreases monotonically with increasing Ti^{4+} content because higher oxidation states shift the absorption edge to higher energy, moving spectral weight away from this window. The $Ti^{4+}/\Sigma Ti$ ratio was subsequently read from the polynomial calibration curve of Zanetta et al. [19]. This approach was preferred over the conventional two-window white-line ratio method because the onset intensity depends solely on the oxidation state and is not affected by crystal-field effects that vary between materials with different crystal chemistry.

Applying this method yields a maximum value of 0.73 and a minimum value of 0.22 for the $Ti^{4+}/\Sigma Ti$ ratio within the (Ti, Ta)O_2 layer. Generally, a higher value is determined in the outer regions of the (Ti, Ta)O_2 and a lower value in the inner regions (Fig. 7c).

Figure 8 shows the shape of the Ta-M4,5 edge in the energy-loss range between 1650 and 2300 eV. It corresponds to those observed in previous studies and indicates + 5 Ta [13, 16]

Scale evolution in time at 1000 °C

Figure 9 shows the oxide scale formed on TaMoCrTiAl during exposure to steam at 1000 °C for 2, 48, 72 and 100 h, respectively. All layers of the external oxide scale described above are already present after 2 h exposure (Fig. 9a). They primarily differ in terms of thickness of the individual layers and additional TiO_2 forming in the IOZ for exposure times > 48 h (Fig. 9b-d). Their corresponding thickness as a function of exposure time is shown in Fig. 10. During the first 72 h of exposure time, an increase in thickness can be observed for all layers of the external oxide scale (Fig. 10b), whereas for the layers (Al, Cr)$_2O_3$, Al_2O_3 and (Ti, Ta)O_2 + Mo, no obvious growth and possibly even a slight decrease in thickness is measured for longer exposure times. However, the TiO_2-layer and the outer sublayer of the (Ti, Ta)O_2 without inclusions keep growing also for those longer exposure times.

The growth rate of the internal oxidation zone thickness appears to be independent of the exposure time, at least up to 100 h (Fig. 10a), but the composition of the internal oxidation zone changes due to the internal TiO_2 precipitates mentioned above. The outer sublayer adjacent to the (Ti, Ta)O_2 is the thickest sublayer after 2 h exposure time (Fig. 9a), but it does not grow significantly if the exposure time is increased. Instead, the thickness of the other two sublayers increases (Fig. 9b-d). The formation of additional Cr_2Ta Laves phase precipitates within the matrix grains

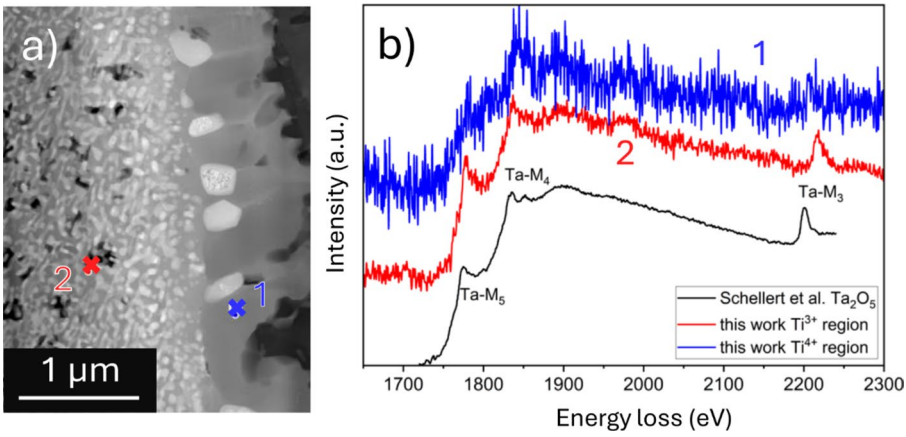

Fig. 8 Results from TEM investigation of complex oxide layers formed on TaMoCrTiAl after 72 h at 1000 °C in steam: **a** STEM-HAADF image with spots of EELS measurements, **b** EELS spectra in the range 1650 to 2300 eV showing Ta-related features along with reference curve taken from [16]

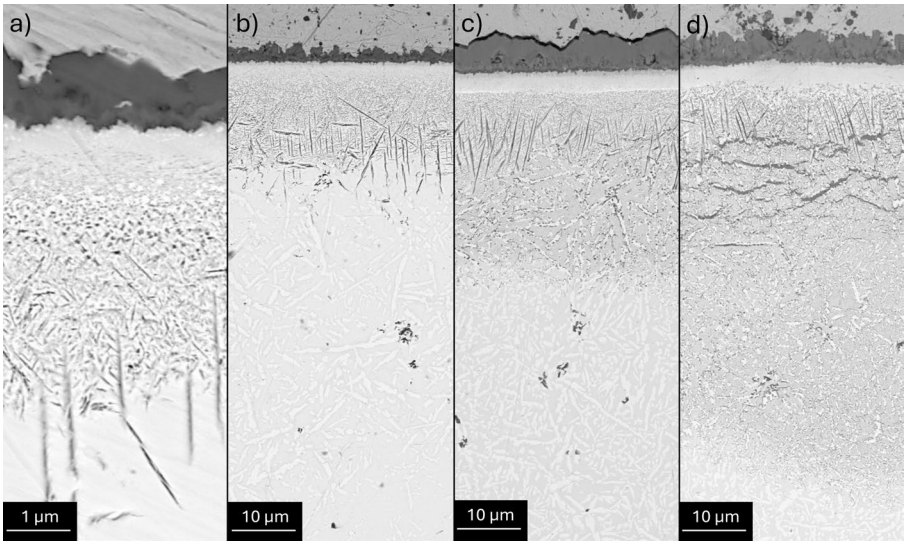

Fig. 9 BSE cross-section images of the oxide scale formed on TaMoCrTiAl after exposure to steam at 1000 °C for **a** 2 h, **b** 48 h, **c** 72 h and **d** 100 h

occurs mostly during the first 48 h (Fig. 9b) and is an intrinsic feature of the alloy [5, 13, 15, 16].

Influence of temperature on the oxidation kinetics

Figure 11 shows cross-sectional BSE images of the oxide scales formed on TaMoCrTiAl during 72 h at 900, 1000 and 1100 °C, respectively. The overall structure of the scales is largely retained in this temperature range with differences lying mainly in the IOZ. The same applies to 1000 °C and varying exposure times. 72 h at 900 °C (Fig. 11a) or 2 h at 1000 °C result in IOZ of similar structure, that do not feature relatively large and elongated Al_2O_3 and no TiO_2 precipitates, which are predominant after 72 h at 1100 °C (Fig. 11c). Numerous large and elongated Al_2O_3 as well as TiO_2 precipitates are also found after 100 h at 1000 °C (Fig. 9d). However, oxide scales and internal oxidation zones are thinner for the respective counterparts at 1000° in both cases. This is also displayed by the area-specific mass change observed during the oxidation experiments, presented in Fig. 12a, showing a lower mass change at 900 °C than at 1000 °C, which in turn is significantly lower than at 1100 °C. The mass gain per unit area $\Delta m/A$ during the isothermal exposure is analysed with the aid of experimental rate-law equation.

$$(\Delta m/A)^n = k_n \cdot t$$

with the exposure time t, the oxidation rate exponent n and oxidation constant k_n. To rule out buoyancy effects, a corresponding reference measurement with an inert dummy sample was performed for each measurement, and the resulting reference $\Delta m/A$ was subtracted from the corresponding experiment curve. From a double-logarithmic plot of mass gain versus exposure time the oxidation rate exponent and

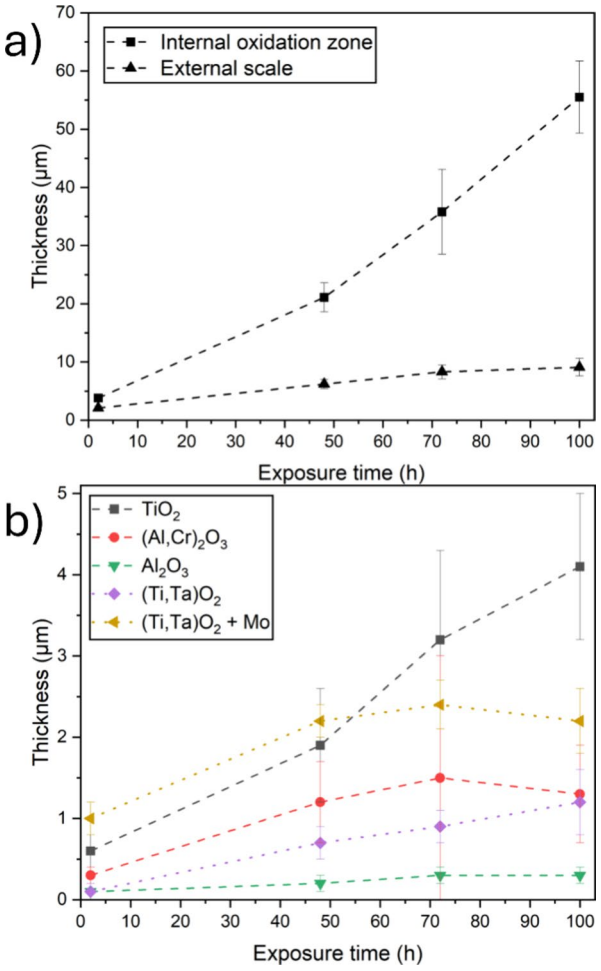

Fig. 10 Thickness of distinguishable layers of corrosion products observed on TaMoCrTiAl depending on the exposure time to steam at 1000 °C. **a** External oxide scale and internal oxidation zone. **b** Individual layers of the external oxide scale

the oxidation constant are derived from linear regression (using the software *Origin*) according to

$$\ln(\Delta m/A) = \frac{1}{n} \ln K_n + \frac{1}{n} \ln t.$$

The time interval used for fitting is selected individually for each curve; it begins approximately at the end of the transient oxidation phase (for example, in the case of 1000 °C, after about 2 hours) and continues until the end of the experiment. Within this time interval, there is no significant change in the rate-law exponent or the oxidation constant observed. The regression analyses yielded R^2 values ≥ 0.990, indicating an excellent fit. The values obtained for n and k_n are listed in Table 2 along with an additional value from the literature for the oxidation of TaMoCrTiAl in air [5]. At 900 and 1100 °C, mass gain complies with an exponential law with exponent around 2 (Table 2), whereas the latter is significantly lower at 1000 °C (1.4), suggesting oxidation kinetics in between linear and parabolic. A relatively small exponent of 1.5 and 1.6 is also observed in the thermogravimetric tests performed at 1000 °c for 48 and

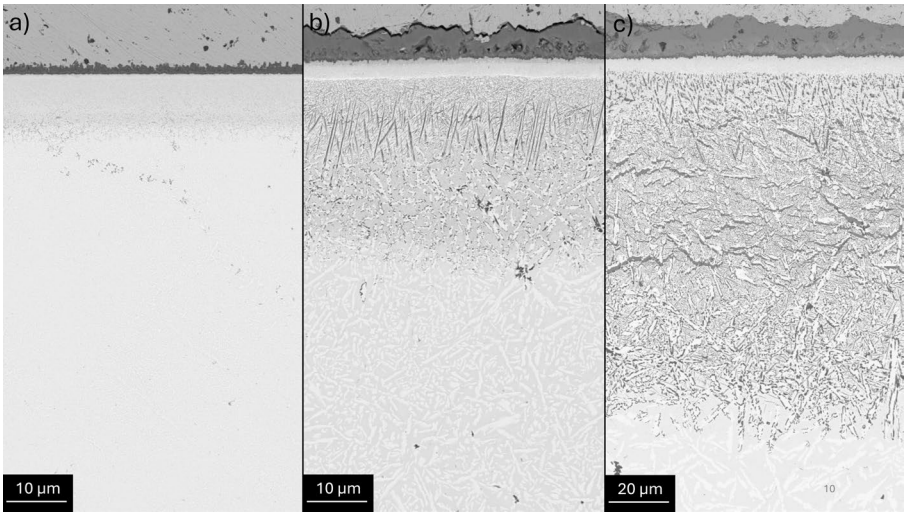

Fig. 11 BSE cross-section images of the oxide scale formed on TaMoCrTiAl after exposure to steam for 72 h at **a** 900 °C, **b** 1000 °C and **c**) 1100 °C

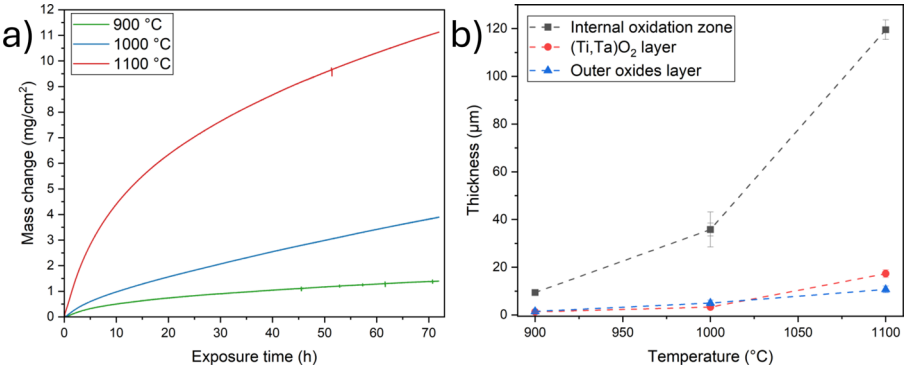

Fig. 12 Oxidation of TaMoCrTiAl during isothermal exposure to steam at 900, 1000–1100 °C: **a** area specific mass change as a function of time, **b** evolution of sublayers of the oxide scale depending on exposure temperature

100 h, respectively. Observing $n = 1.8$ for oxidation of TaMoCrTiAl at 1000 °C in air in two different laboratories (Table 2) raises the confidence that the deviation of 0.2 from the expectation of parabolic mass change ($n = 2$) is significant in the sense that the precision of thermogravimetric tests is generally high enough to reveal such. The results of repeated testing at 1000 °C in steam likewise corroborate a reproducibility of n within the range of +/- 0.1.

Figure 12b shows the thickness of IOZ, (Ti, Ta)O_2 layer and outer oxide layer (TiO_2, (Al, Cr)$_2O_3$ and Al_2O_3) for 900, 1000 and 1100 °C after 72 h exposure each. Whilst at 900 °C the two layers of the external scale possess roughly the same thickness, at 1000 °C the outer oxide layer is slightly thicker. At 1100 °C, this is reversed

Table 2 Rate-law exponent n, (parabolic) rate constant k_n and mass gain after 72 h observed for oxidation of TaMoCrTiAl in steam at 900, 1000–1100 °C, respectively or in synthetic air at 1000 °C

Atmosphere	Temperature (°C)	*n* (-)	k_n (10^{-2} $mg^2cm^{-4}h^{-1}$)	Mass gain, 72 h (mg cm^{-2})	Reference
air	1000	1.8	2.7	1.46	This study
air	1000	1.8	3.3		[5]
steam	900	1.9	2.7	1.39	This study
steam	1000	1.4	9.5	3.89	This study
steam	1100	2.0	195.4	11.12	This study

and the layer of the complex oxide is significantly thicker. At all temperatures, the IOZ is by far the thickest layer.

Results of oxidation experiment with Pt marker

Figure 13 exemplifies the position of the Pt markers within the oxide scale formed after 48 h at 1000 °C. They are located within the upper sublayer of the (Ti, Ta)O_2 close to the bigger Mo inclusions. This indicates that the layers TiO_2, (Al, Cr)$_2O_3$, Al_2O_3 and (Ti, Ta)O_2 without inclusions grow mainly through cation outward diffusion, whereas the layer below ((Ti, Ta)O_2 + Mo) grows predominantly due to anion inwards diffusion. Accordingly, the band of bigger Mo inclusions can be roughly regarded as an indicator for the position of the original alloy surface.

Results of discontinuous oxidation experiment

Figure 14 shows the results of the discontinuous oxidation experiment, which was additionally performed to identify the diffusion fluxes through the oxide scale and assess the findings observed during the Pt experiment. Figure 14a illustrates the sample with removed outer oxide layers (rutile TiO_2, (Al, Cr)$_2O_3$ and Al_2O_3), while Fig. 14b shows the external oxide scale formed after the second oxidation stage (1000 °C, 24 h) along with corresponding EDX elemental mapping in Fig. 14c. After the second oxidation step the general structure of the external oxide scale as described previously is restored (Fig. 14b), which confirms the outwards diffusion of Ti, Cr and Al through the (Ti, Ta)O_2 scale.

However, although the general structure of the oxide layer is rebuilt after the second oxidation step, the respective thicknesses of the individual layers and their chemical composition differ from those formed during the continuous experiments. The newly formed outer oxide scale contains reduced amounts of Ti and Al. Instead of a continuous TiO_2 layer, only isolated TiO_2 grains are observed, forming a discontinuous layer above a significantly Cr-richer (Al, Cr)$_2O_3$ layer. Additionally, the formation of the Al_2O_3 layer is also less pronounced (Fig. 13c).

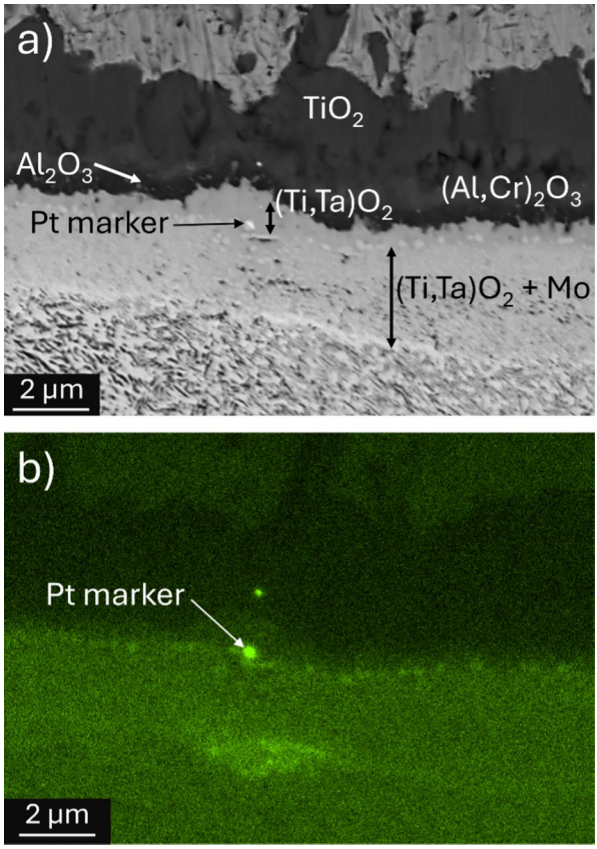

Fig. 13 **a** BSE cross-section image showing the Pt marker within the upper sublayer of the (Ti, Ta)O_2 and **b** corresponding EDX mapping for Pt

Discussion

Oxidation mechanism of TaMoCrTiAl in steam

Both the Pt-marker and the discontinuous oxidation experiments suggest that the outer oxide layers (TiO_2, (Al, Cr)$_2O_3$ and Al_2O_3) grow by cation outward diffusion. TiO_2 layers are comparatively thick (Fig. 10b), corresponding outward diffusion of Ti, outweighing diffusion Cr or Al. The position of Pt-markers also point to outward growth of the (Ti, Ta)O_2 sub-layer that does not feature Mo inclusions, which then is likely to be limited by the outward diffusion of Ta, which has been reported to be rather low [20, 21]. Such imbalance between Ti and Ta diffusion in (Ti, Ta)O_2 may also explain their non-uniform distribution across the complex oxide, i.e. higher Ti content in the outer, Mo-free sub-layer part and higher Ta content in the inner part (Fig. 4b).

The inner part of the layer (Ti, Ta)O_2 grows predominantly via oxygen inwards diffusion, which complies with the presence of metallic Mo inclusions in this sub-layer. Volatilization in the form of MoO_3 is an option in both air and steam environments [5, 14, 22, 23], however, only direct contact of Mo with the atmosphere, consistent with the relatively low standard Gibbs free energy of MoO_3 formation

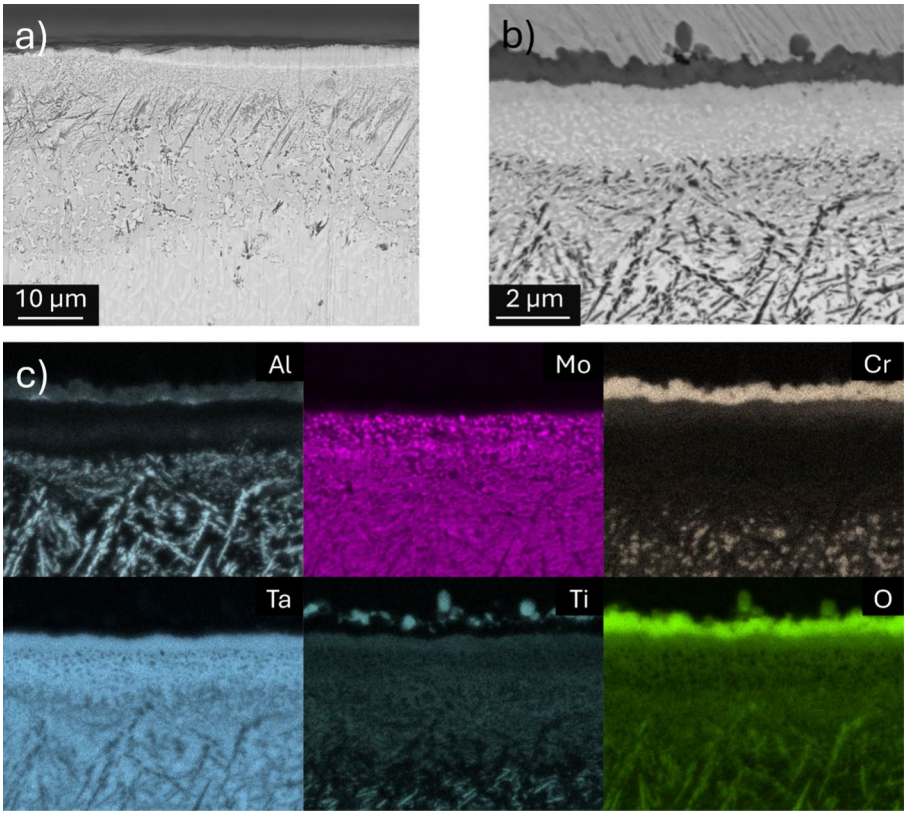

Fig. 14 Discontinuous oxidation experiment: **a** BSE cross-section image of the oxide scale after removal of the outer scale, **b** BSE cross-section image of the oxide scale after the second oxidation step, **c** EDX elemental maps corresponding to (**b**)

Table 3 Standard free energy of formation of relevant oxides at 1000 °C [5, 21]

Oxide	Cr_2O_3	Ta_2O_5	TiO_2 (rutile)	Al_2O_3	MoO_3	(Cr, Ta, Ti)O_2	(Ti, Ta)O_2
ΔG^0 (kJ/mole O_2)	-538	-598	-713	-853	-293	-640	-685

(Table 3). While this may occur in the porous outer oxide layers, the dense (Ti, Ta)O_2 effectively blocks further volatilization once it has formed a continuous layer. As a result, Mo becomes trapped beneath this layer, remains metallic and form discrete inclusions to minimize interfacial energy. Segregation at interfaces to the localised Mo enrichment, e.g. apparent from Fig. 4b. Similarly, Al_2O_3 inclusions observed in the inner (Ti, Ta)O_2 sub-layer are interpreted as remnants of earlier formed internal precipitates that were subsequently engulfed by the inward-growing complex oxide. The formation of the internal oxidation zone itself is driven by the lower Gibbs free energy of formation of both Al_2O_3 and TiO_2 compared to (Ti, Ta)O_2 (Table 3) along with the oxygen solubility in TaMoCrTiAl.

The IOZ, in turn, influences the diffusion processes and thus the growth behaviour of the external scale. The formation of internal Al_2O_3 and TiO_2 precipitates causes a

significant decrease in the flux of these elements from the alloy reaching the external scale. In case of Al, this effect occurs almost from the very beginning and prevents the formation of a closed Al_2O_3 layer, whereas in the case of Ti, it is delayed and only takes full effect once the massive formation of internal TiO_2 precipitates has begun. At 1000 °C this happens after approximately 72 h. This delay is caused, on the one hand, by the higher Gibbs free energy of formation of TiO_2 compared to Al_2O_3 (Table 3), and on the other hand, by the depletion of metallic Ti in the alloy in a region immediately beneath the external scale. As the oxidation proceeds, the partial pressure of oxygen increases in areas deeper inside the alloy which are not depleted in Ti and finally reaches a level that allows TiO_2 to form, leading to the massive internal TiO_2 formation observed in some distance from the external scale (Fig. 9d). The progressive depletion of Ti in the alloy matrix, caused by continued outward diffusion towards the outer TiO_2 layer, consequently reduces the inward growth rate of the (Ti, Ta)O_2 layer (Fig. 10b).

Based on the above considerations, the oxidation process of TaMoCrTiAl in pure steam can be divided into three stages, which are schematically summarized in Fig. 15. First, a transient oxidation stage in which the general structure of the oxide layer forms and that ends with the formation of a continuous (Ti, Ta)O_2 layer. Second, an intermediate stage in which, on the one hand, the outer layers of the oxide scale grow due to outward diffusion of Ti, Cr and Al, while, on the other hand, the (Ti, Ta)O_2 layer and Al_2O_3 precipitates inside the IOZ grow due to the inward diffusion of oxygen. And finally, a third phase characterised by significantly enhanced formation of internal TiO_2 precipitates and correspondingly decreased growth of the external scale.

Rate laws observed for mass gain

Although the general structure of the oxide scales found after exposure for 72 h at 900, 1000, and 1100 °C is quite similar, the exponential rate laws on the basis of mass

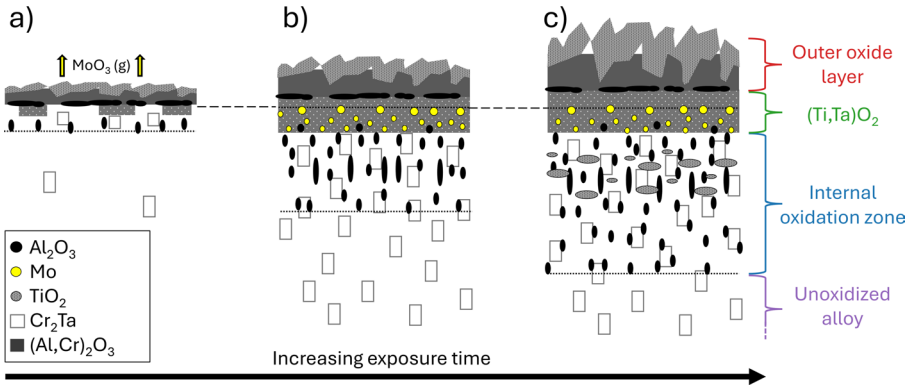

Fig. 15 Schematic illustration of the oxidation mechanism of TaMoCrTiAl during exposure at 1000 °C in pure steam: **a** transient oxidation stage, **b** early oxidation stage with internal Al_2O_3 formation and growth of external oxide scale and **c** later oxidation stage with internal Al_2O_3 and TiO_2 formation and decreased growth rate of external oxide scale

change (gain) inferred from the tests show different exponents (Table 2). An exponent of $n = 1.9$ as observed for steam environment at 900 °C might still have to be understood as a parabolic mass gain, controlled in rate by diffusion of cations or anions across a growing layer within the complicated oxide scale [14]. a parabolic oxidation kinetic at 900 °C, which is usually associated with diffusion, either of cations or anions, through a layer that increases in thickness parabolically as the rate-determining step (i.e., the slowest step) [14]. However, 1.4 to 1.6 found for the exposure to steam at 1000 °c is here regarded as a significant deviation from the parabolic rate law. The formation of volatile oxidation products cannot easily explain exponential mass gain with exponent < 2, as, because of superimposed mass loss, mass gain recorded in a thermogravimetric test abates faster than expected from a gradually developing diffusion barrier, i.e. n should rather be > 2. A generic, independent of alloy or environment, explanation of $n < 2$ in mass-gain curves follows from the necessary prerequisites for observing a parabolic rate law, notably that all the mass that still passes the growing layer of a corrosion product, irrespective of whether metal or non-metal primarily diffuse, contributes exclusively to the growth of this layer. Otherwise, the instantaneous gain in mass will be higher than corresponds to the increase in thickness of the diffusion barrier, and the subsequent decrease of the rate of mass gain will be less than expected of a parabolic rate law, which is what $n < 2$ finally means. For TaMoCrTiAl exposed to steam at 1000 °c, the candidate for the growing diffusion barrier may be (Ti, Ta)O_2, including both sub-layers, with oxygen and Ti being additionally consumed by growth of the IOZ and outer TiO_2, respectively (Fig. 10). If so, these two layers in the scale should grow linearly in thickness once the (Ti, Ta)O_2 approaches a constant thickness, with which the measurements presented in Fig. 10 at least approximately comply. At 1100 °C, mass gain of TaMoCrTiAl in the presence of steam again follows a parabolic rate law (Table 2) but on a level of mass gain that clearly corresponds to the higher temperature (Fig. 12a). In the spirit of the discussion above, this means that transport across the predominantly growing layer inside the oxide scale limits the mass gain, for which, in this case, the IOZ (Figs. 11c and 12b) may be regarded as the primary candidate. It should be noted that $n = 1.8$ for mass gain of TaMoCrTiAl in air, confirmed in tests in two laboratories (Table 2), may also result from simultaneous growth of at least two layers. While the different exponents in the observed rate laws may generally be understood in this way, the non-ambiguous assignment of specific roles to the layers of the oxide scale must be left for future work.

Comparison to oxidation in air

Figure 16 exemplifies the oxidation behaviour of TaMoCrTiAl after exposure to steam and synthetic air at 1000 °C for 72 h, whereas the latter has been already investigated in more detail previously [5, 13, 16]. During oxidation in air and steam, the oxide scale exhibits a similar general structure: a porous outer layer composed of TiO_2 and Al-Cr-based oxides, underlain by a layer of complex rutile-type oxide containing metallic Mo inclusions in its lower part, followed by a thick internal corrosion zone including Al_2O_3 and Ti-containing precipitates. Despite the clear similarities in the oxidation behaviour, there are nevertheless some differences if TaMoCrTiAl is

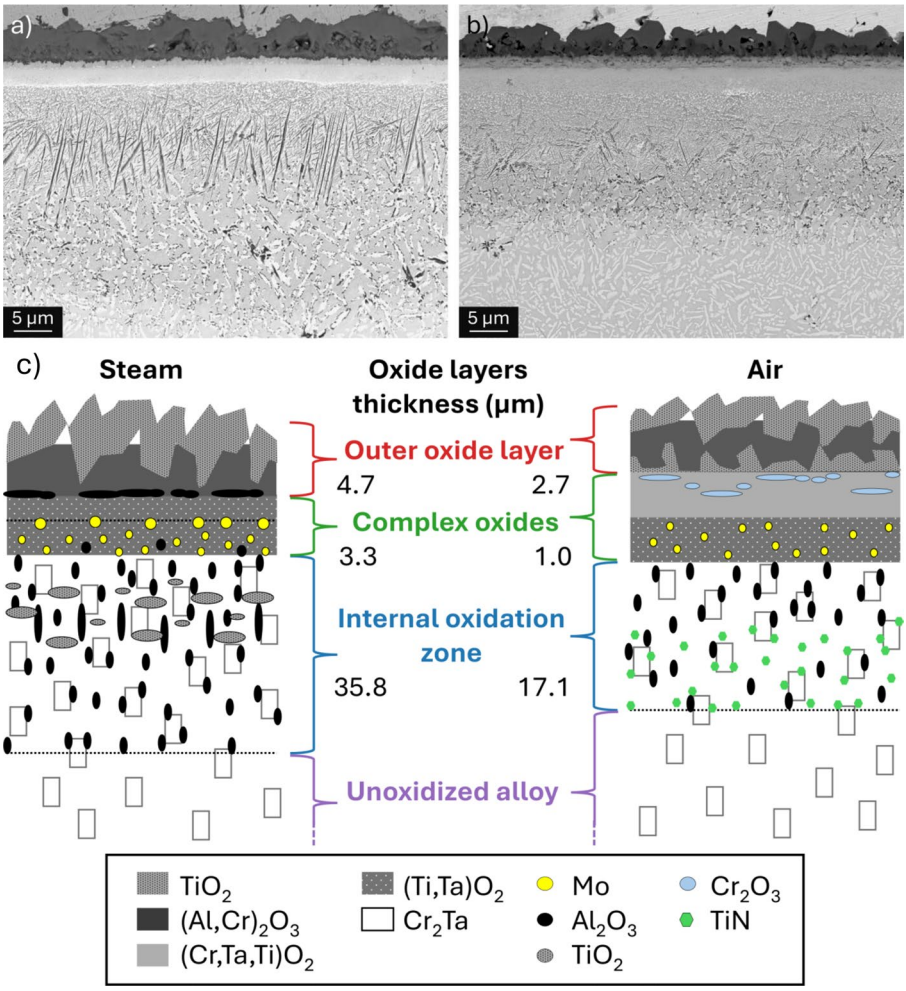

Fig. 16 Oxide scales formed on TaMoCrTiAl at 1000 °C after 72 h exposure to **a** steam and **b** synthetic air; **c** schematic representation of the respective oxide scales and thicknesses of their sublayers

exposed to steam: (1) an overall thicker oxide scale for both external scale (8.0 vs. 3.7 µm) and internal corrosion zone (35.8 vs. 17.1 µm),; (2) the rutile-type complex oxide layer exhibits reduced porosity and lacks Cr incorporation, i.e., no formation of (Cr, Ta, Ti)O_2 or Cr_2O_3 precipitates; (3) a thin discontinuous Al_2O_3 layer between the outer part of the scale and the complex oxide; (4) TiO_2 instead of TiN precipitates in the internal corrosion zone accompanied by coarse precipitate morphology.

The absence of the (Cr, Ta, Ti)O_2 layer in steam is regarded as the most decisive difference, as this phase has been identified as the primary contributor to the high oxidation resistance of TaMoCrTiAl in air, particularly through its ability to effectively suppress outward cation diffusion and the formation of deleterious Ta_2O_5 [4, 5]. In contrast, no comparable barrier properties but only mitigation of Ta_2O_5 formation is reported for (Ti, Ta)O_2 [20, 21]. The limited ability of (Ti, Ta)O_2 to restrict

outward cation transport is further supported by the discontinuous oxidation experiments conducted in this study. In contrast to oxidation in air [5], continued growth of the outer oxide layer is observed, indicating enhanced cation mobility in (Ti, Ta)O_2. This behaviour is likely to be associated with changes in the defect chemistry of the rutile-type complex oxide, particularly an increased concentration of cation vacancies. Such an interpretation is consistent with the observed Ti-valence gradient across the (Ti, Ta)O_2 layer. In the outer region, where the Ti/Ta ratio exceeds one, Ti exhibits a maximum valence of 3.73, which gradually decreases to 3.22 toward the inner region, where the Ta content increases. In both (Ti, Ta)O_2 and the corresponding (Cr, Ta, Ti)O_2 phase formed during oxidation in air, Ta retains a valence of +5, as demonstrated by EELS measurements in the present and a previous study [13]. Consequently, the average cation valence exceeds the nominal value of +4 required for a stoichiometric MO_2 rutile structure. An increased concentration of cation vacancies would provide a mechanism to compensate this excess positive charge while simultaneously facilitating outward cation diffusion.

While this hypothesis may rationalize the inferior protective properties of (Ti, Ta)O_2 relative to (Cr, Ta, Ti)O_2, it does not explain the absence of the latter phase during oxidation in steam. Cr volatilization in the form of oxy-hydroxide seems rather unlikely, as significant formation of this volatile Cr compound requires the relatively high oxygen partial pressure such as prevailing in wet air [14]. Furthermore, the Cr-rich outer oxide layer especially observed in the discontinuous oxidation experiment contradicts loss of Cr to the environment.

Instead, the absence of (Cr, Ta, Ti)O_2 in steam may be rationalized by the higher thermodynamic stability of TiO_2 and Ta_2O_5 compared to Cr_2O_3 (Table 3), in view of the low oxygen partial pressure in steam produced from deaerated water. This lower oxygen partial pressure may favour the preferential formation of (Ti, Ta)O_2 during the transient stage, thereby suppressing the development of a (Cr, Ta, Ti)O_2 layer once a continuous rutile layer is established. Not least, (Cr, Ta, Ti)O_2 could actually have formed but decomposed into (Ti, Ta)O_2 and Cr_2O_3. Evidence of such decomposition is provided by the formation of Cr_2O_3 within the complex oxide during prolonged oxidation in air [13].

The lack of TiN in the internal oxidation zone is due to the significantly lower N content (only present as impurity) of the reactive gas. Instead, TiO_2 is formed. The increased mass gain and thickness of the internal oxidation zone for oxidation in steam is in line with similar findings for the oxidation of Ti-based alloys in wet atmospheres [6–12]. Galerie et al. explain this observation with the more rapid inwards diffusion of OH^- ions via oxygen vacancies of the external rutile TiO_2 scale due to their lower charge and size and, therefore, a reduced activation energy for the diffusion process [8]. This effect could also apply to rutile-type oxides formed on TaMoCrTiAl and thereby further enhance the inward oxygen flux.

Conclusions

The oxidation behaviour of TaMoCrTiAl in steam at 900–1100 °C has been investigated. The main conclusions are summarized as follows:

- Oxidation in steam leads to a multilayered oxide scale: a TiO_2-rich layer with (Al, Cr)$_2O_3$/Al_2O_3 at the interface to the steam, followed by rutile-structured (Ti, Ta)O_2 in tow sub-layers and a pronounced IOZ including Al_2O_3 and TiO_2. Metallic Mo precipitates inside the inner (Ti, Ta)O_2 sub-layer.
- Both inward diffusion of oxidizing species and outward diffusion of metal cations are significant. After establishment of the (Ti, Ta)O_2 layer, oxidation becomes dominated by anion diffusion.
- Mass gain is approximately parabolic at 900 and 1100 °C. At 1000 °C, mass gain follows an exponential rate law with exponent between 1.4 and 1.6. According to layer thickness, internal oxidation is the dominant degradation pathway.
- In contrast to oxidation in synthetic air, (Cr, Ta, Ti)O_2 is absent in the scale. The presence of apparently less protective (Ti, Ta)O_2 result in both significantly thicker external oxide and more pronounced internal corrosion.

Author contributions B.S. wrote the main manuscript text. All authors reviewed the manuscript.

Funding Open Access funding enabled and organized by Projekt DEAL. This study was supported by the Deutsche Forschungsgemeinschaft (DFG) under grant number 467750555.

Data availability The data that support the findings of this study are available from the corresponding author upon reasonable request.

Declarations

Conflict of interest The authors declare no conflicts of interest.

References

1. O.N. Senkov, G.B. Wilks, D.B. Miracle, C.P. Chuang, P.K. Liaw, Refractory high-entropy alloys, Intermetallics 18 (2010) 1758–1765.
2. W. Xiong, A.X.Y. Guo, S. Zhan, C.T. Liu, S.C. Cao, Refractory high-entropy alloys: a focused review of preparation methods and properties, J. Mater. Sci. Technol. 142 (2023) 196–215.
3. B. Gorr, S. Schellert, F. Müller, H.-J. Christ, A. Kauffmann, M. Heilmaier, Current status of research on the oxidation behavior of refractory high entropy alloys, Adv. Eng. Mater. 23 (2021) 2001047.
4. B. Gorr, F. Müller, S. Schellert, H.-J. Christ, H. Chen, A. Kauffmann, M. Heilmaier, A new strategy to intrinsically protect refractory metal based alloys at ultra high temperatures, Corros. Sci. 166 (2020) 108475.
5. F. Müller, B. Gorr, H.-J. Christ, J. Müller, B. Butz, H. Chen, A. Kauffmann, M. Heilmaier, On the oxidation mechanism of refractory high entropy alloys, Corros. Sci. 159 (2019) 108161.

6. B. Öztürk, M. Rudolphi, E. M. White, D. Dickes, U. Glatzel, M. C. Galetz, Influence of Water Vapor on the Oxidation of Pure Titanium, High Temp. Corros. Mater. 101 (2024) 1341–1351.
7. B. Öztürk, L. Mengis, D. Dickes, U. Glatzel, and M. C. Galetz, Influence of water vapor and temperature on the oxide scale growth and alpha-case formation in Ti–6Al–4V alloy, Oxid. Met. 97 (2022) 241.
8. A. Galerie, Y. Wouters, and M. Caillet, The kinetic behaviour of metals in water vapour at high temperatures: can general rules be proposed?, Mater. Sci. Forum 231 (2001) 369–372.
9. F. Motte, C. Coddet, P. Sarrazin, M. Azzopardi, and J. Besson, A comparative study of the oxidation with water vapor of pure titanium and of Ti–6Al–4V, Oxid. Met. 10 (1976) 113.
10. P. Perez, On the influence of water vapour on the oxidation behaviour of pure Ti, Corros. Sci. 49 (2007) 1172.
11. M. Gobel, J. D. Sunderkotter, D. I. Mircea, H. Jenett, and M. F. Stroosnijder, Study of the high-temperature oxidation behaviour of Ti and Ti4Nb with SNMS using tracers, Surf. Interface Anal. 29 (2000) 321–324.
12. Y. Wouters, A. Galerie, and J.-P. Petit, Thermal oxidation of titanium by water vapour, Solid State Ion. 104 (1997) 89.
13. B. Schäfer, M. Dürrschnabel, C. Schroer, F. Lanoy, E. White, M. Galetz, C. Tang, B. Gorr, Effect of Re or W addition on the oxidation behaviour of a compositionally complex Ta–Mo–Cr–Ti–Al alloy in air at 1000°C, Mater. Corros. 1 (2026) 12.
14. D. Young, High temperature oxidation and corrosion of metals, Elsevier, 2008.
15. S. Schellert, B. Gorr, S. Laube, A. Kauffmann, M. Heilmaier, H.J. Christ, Oxidation mechanism of refractory high entropy alloys Ta–Mo–Cr–Ti–Al with varying Ta content, Corros. Sci. 192 (2021) 109861.
16. S. Schellert, M. Weber, H.J. Christ, C. Wiktor, B. Butz, M.C. Galetz, S. Laube, A. Kauffmann, M. Heilmaier, B. Gorr, Formation of rutile $(Cr,Ta,Ti)O_2$ oxides during oxidation of refractory high entropy alloys in Ta–Mo–Cr–Ti–Al system, Corros. Sci. 211 (2023) 110885.
17. E. Stoyanov, F. Langenhorst, G. Steinle-Neumann, The effect of valence state and site geometry on Ti $L_{3,2}$ and O K electron energy-loss spectra of Ti_xO_y phases, Am. Mineral. 92 (2007) 577–586.
18. L.F. Kourkoutis, H. L. Xin, T. Higuchi, Y. Hotta, J.H. Lee, Y. Hikita, D.G. Schlom, H.Y. Hwang, D.A. Mueller, Atomic resolution spectroscopic imaging of oxide interfaces, Philos. Mag. 90 (2010) 4731–4749.
19. P.-M- Zanetta, V. R. Manga, Y.-J. Chang, T. Ramprasad, J. Weber, J. R. Beckett, T. J. Zega, Atomic-scale characterization of the oxidation state of Ti in meteoritic hibonite: Implications for early solar system thermodynamics, Am. Mineral. 108 (2023) 881–902.
20. N. J. Welch, M. J. Quintana, T. M. Butler, P. C. Collins, High-temperature oxidation behavior of TaTiCr, Ta4Ti_3Cr, and Ta_4TiCr_3 concentrated refractory alloys, J. Alloys Comp. 941 (29023) 169000.
21. N. J. Welch, M. J. Quintana, S. J. Kuhr, T. M. Butler, P. C. Collins, Intermediate and high-temperature oxidation of an equiatomic TaTiCr RCCA from 800°C to 1400°C, Int. J. Refract. Met. Hard Mater. 118 (2024) 106437.
22. E.A. Gulbransen, K. F. Andrew, F. A. Brassart, Oxidation of Molybdenum 550° to 1700°C, J. Electrochem. Soc. 110 (1963) 952.
23. A.T. Nelson, E.S. Sooby, Y.-J. Kim, B. Cheng, S.A. Maloy, High temperature oxidation of molybdenum in water vapor environments, J. Nucl. Mater. 448 (2014) 441–447.

Authors and Affiliations

Björn Schäfer[1] · Michael Dürrschnabel[1] · Carsten Schroer[1] · Chongchong Tang[1] · Fabian Lanoy[2] · Emma White[2] · Mathias Galetz[2] · Bronislava Gorr[1]

✉ Björn Schäfer
bjoern.schaefer@partner.kit.edu

Michael Dürrschnabel
michael.duerrschnabel@kit.edu

Carsten Schroer
carsten.schroer@kit.edu

Chongchong Tang
chongchong.tang@kit.edu

Fabian Lanoy
fabian.lanoy@dechema.de

Emma White
emma.white@dechema.de

Mathias Galetz
mathias.galetz@dechema.de

Bronislava Gorr
bronislava.gorr@kit.edu

[1] Institut für Angewandte Materialien, Karlsruher Institut für Technologie (KIT), Karlsruhe, Germany

[2] Dechema-Forschungsinstitut, Frankfurt, Germany